Testing interaction models by using x-ray absorption spectroscopy: solid Pb

2002 J. Phys.: Condens. Matter 14 3365

(http://iopscience.iop.org/0953-8984/14/12/321)

INSTITUTE OF PHYSICS PUBLISHING JOURNAL OF PHYSICS: CONDENSED MATTER

J. Phys.: Condens. Matter **14** (2002) 3365–3382 PII: S0953-8984(02)30979-2

Testing interaction models by using x-ray absorption spectroscopy: solid Pb

Andrea Di Cicco[1], **Marco Minicucci**[1], **Emiliano Principi**[1], **Agnieszka Witkowska**[2,3], **Jaroslaw Rybicki**[2,3] **and Robert Laskowski**[2]

[1] INFM, Dipartimento di Fisica, Università di Camerino, Via Madonna delle Carceri, I-62032 Camerino (MC), Italy
[2] Department of Solid State Physics, Technical University of Gdansk, Narutowicza 11/12, 90-857 Gdansk, Poland
[3] TASK Computer Centre, Technical University of Gdansk, Narutowicza 11/12, 90-857 Gdansk, Poland

Received 20 November 2001
Published 15 March 2002
Online at stacks.iop.org/JPhysCM/14/3365

Abstract

Structural models obtained using classical molecular dynamics (MD) simulations and realistic interatomic potentials for solid metals are tested using experimental results obtained by x-ray absorption spectroscopy (XAS). Accurate L-edge extended x-ray absorption fine-structure (EXAFS) measurements of Pb grains dispersed in BN and graphite matrices have been collected for temperatures up to the melting point. The thermal expansion of the grains was measured by energy-dispersive x-ray diffraction techniques and found to be coincident with that of pure Pb up to the limit of the present measurements. L_3-edge EXAFS measurements of solid Pb at various temperatures have been analysed using advanced data-analysis techniques (GNXAS) based on exact spherical-wave multiple-scattering simulation of the absorption cross-section. Realistic structural models for solid Pb were obtained from MD simulations using an empirical pair potential (Dzugutov, Larsson and Ebbsjo (DLE)), a tight-binding (TB) square-root functional, and an embedded-atom (EA) model potential parametrized by us. The short-range pair distribution function $g(r)$ reconstructed by means of EXAFS is compared with those obtained by MD simulations. The empirical DLE potential, originally designed for the liquid state, is too soft, showing too-large values for the average distance R, variance σ^2, and skewness β. The TB and EA potentials are both compatible with XAS data as regards the average distance and skewness of the first neighbours. The distance variance, associated with the thermal vibration amplitudes, is underestimated for the TB potential, while the EA model is found to be in agreement with XAS data. The present results are also compared with those from a previous EXAFS study on solid lead, where the cumulant expansion and a simple one-dimensional anharmonic oscillator model were used. The need for realistic interaction models and appropriate simulation schemes for reliable XAS data analysis is emphasized, while differences from and improvements with respect to previous approaches are only briefly discussed.

1. Introduction

In recent times, x-ray absorption spectroscopy (XAS) has proved to be very useful for investigating short-range interaction properties in various condensed systems. Effective two-body potentials describing the interatomic interaction in noble gases were tested for krypton at high pressure [1] and low temperature [2] using XAS and Monte Carlo simulations. The accuracy of present theoretical models for the interatomic potential in solid and liquid simple ionic systems was discussed in [3, 4] on the basis of a direct comparison between XAS and molecular dynamics (MD) results. For those systems, XAS was shown to be sensitive to fine details of the effective potential, and quantitative information about deviations from the simple harmonic approximation was obtained using model asymmetric functions for the pair distribution or the cumulant expansion.

The inadequacy of the harmonic approximation in describing thermal vibrations, especially at high temperatures, has been studied in several other cases including those of metals (see [5, 6] and references therein) and superionic salts (see [7, 8] and references therein). In particular, detailed studies of simple solid metals at high temperature such as Cu [5] and Rh [6, 9] have shown that a deep insight into the atomic interaction can be gained by looking at the evolution of the low-order cumulants of the first-shell distribution as a function of temperature. In a recent paper [10], it has been shown that the shape of an effective pair potential describing the interatomic interaction in MD simulations of solid Rh can be refined using first-neighbour pair distribution functions determined by XAS at various temperatures.

In the present paper we intend to test current interatomic interaction models using Pb L-edge XAS measurements as a function of temperature. Previously, Stern *et al* [11] reported an XAS study of solid lead at several temperatures up to the melting point. Standard data analysis was used to measure the first four cumulants of the first-neighbour distribution, showing that it is possible to reconstruct the radial distribution using a simple one-dimensional anharmonic oscillator. However, no direct comparison with simulations of the structure obtained using established interaction models for solid metals was presented. For solid metals, the most widely used interaction models are the embedded-atom (EA) potentials [12–15], Finnis and Sinclair (FS) potentials [16] corresponding to the second-moment approximation within the tight-binding (TB) scheme, and Sutton and Chen (SC) potentials [17, 18]. All the aforementioned classes of potentials are of many-body type, and allow one to reproduce basic features of metallic systems including the experimental finding that for most cubic crystals $C_{12} \neq C_{44}$ (Cauchy discrepancy), a fact that cannot be explained using pairwise-additive potentials. In particular, a new parametrization method for EA potentials, based on an inversion technique, is briefly described in the present paper.

Here, we use advanced *ab initio* XAS data-analysis techniques (GNXAS [19–21]) including double-electron-excitation channels [22] in the atomic background for analysing good quality L_3-edge data over an extended energy range. Absolute distance values and a consistent reconstruction of the pair distribution function with no assumptions about the potential form are possible using this method. In particular, pair distribution functions can be directly compared with our MD results obtained using realistic potentials for fcc metal systems, allowing us to study the details of the interaction. The aim of this work is twofold. On the one hand, we want to compare accurate XAS short-range structural results with classical MD simulations obtained using realistic potentials for fcc metal systems. This allows us to evaluate the accuracy of different interaction functionals, including the new EA model presented in this paper, corresponding to different local structural models. On the other hand, we provide a detailed comparison with previous XAS results [11] obtained using standard data analysis and

a simple one-dimensional effective interaction, with the aim of showing the improvements and capabilities of the new GNXAS and the deep insight given by the comparison with realistic structural models.

2. Experimental procedure

Samples of solid and liquid lead suitable for high-temperature measurements were prepared starting from micrometric powders of PbO mixed with appropriate quantities of BN or graphite. The powders were carefully mixed and then pressed to form pellets. Pellets were loaded in suitable furnaces for x-ray absorption fine-structure (XAFS) measurements [23] under high-vacuum conditions and treated *in situ* following the reduction process which takes place at high temperatures, using a graphite crucible. The reduction process, monitored using x-ray diffraction and XAFS, begins at about 300 °C and is completed within a few minutes at about 600 °C. The final samples were constituted of dispersions of submicrometric Pb grains (the average size is in the range 0.5–1 μm) into BN (Pb–BN specimens) or graphite (Pb–C specimens) matrices.

The purity of the final Pb metal powdered sample was checked by looking at the x-ray diffraction peaks and at the Pb L-edge XAFS patterns which have been found to reproduce those of Pb 10 μm films deposited under vacuum conditions [11,22]. X-ray diffraction patterns of the Pb–C samples were collected as a function of temperature at the DW11A beamline at the LURE laboratories (Orsay) using the energy-dispersive x-ray diffraction (EDXD) configuration. A modified version of the furnace, adapted to that experimental set-up, was installed for this purpose during dedicated beam time. Energy-scanning x-ray diffraction (ESXD) patterns of Pb–BN samples were also collected at the ESRF (BM29 beamline) using the advanced set-up which allows simultaneous XAFS and ESXD measurements [24].

A typical energy-dispersive diffraction pattern containing the (111), (200), (220), (311), and (222) Pb Bragg peaks for graphite pellets containing Pb grains is shown in figure 1. The diffraction pattern has been simulated using Gaussian peaks and a polynomial background, excluding the 24.5–31 keV energy region which contains only the graphite (100) and (101) Bragg peaks (the weak (004) peak of graphite has been included in the simulation). The angle has been separately measured using a Cu standard, so the position of the Bragg peaks is only related to the cell parameter a. The quality of the refinement can be appreciated looking at the lower panel of figure 1 showing the difference between the logarithms of the experimental and calculated patterns.

The thermal expansion of the Pb grains obtained by reducing PbO in graphite pellets is measured using this technique and the present results (⊡) in the 70–270 °C temperature range are compared with the accepted thermal expansion curve [25] of solid Pb in figure 2. The results obtained by measuring the Pb(111) peak position at the ESRF as a function of temperature for similar Pb–BN samples are also reported in figure 2 (⋄). The present results reproduce the previous determination of the thermal expansion in the temperature range [25] under consideration. Thus, both types of Pb dispersion used in this work are representative of bulk Pb samples.

The XAFS spectra of solid lead at the L_3, L_2, and L_1 edges have been recorded at the BM29 beamline at the European Synchrotron Radiation Facility (Grenoble), using a double-crystal monochromator equipped with Si(311) crystals. The measurements were performed using a furnace adapted to making combined XRD/XAFS measurements for several temperatures below the Pb melting point (327): 26, 79, 101, 150, 210, and 260 °C, in the energy range 12.9–14.0 keV (the Pb L_3-edge energy amounts to about 13.035 keV). Figure 3 shows the absorption spectra of solid lead recorded at the L_3 edge as a function of the temperature in

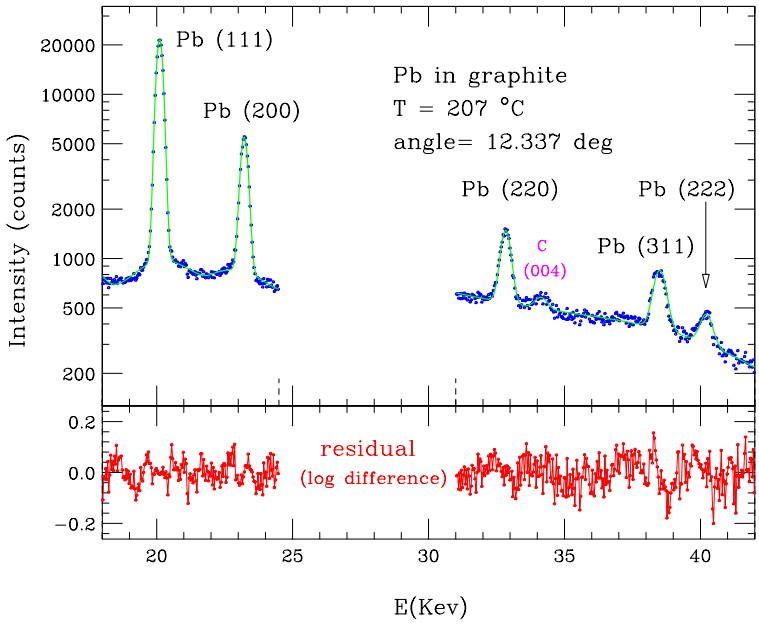

Figure 1. Upper panel: experimental (dots) and simulated EDXD patterns of Pb in graphite ($T = 207\,^{\circ}$C). Lower panel: the difference between the logarithms of the experimental and calculated patterns.

(This figure is in colour only in the electronic version)

the near-edge region. The amplitude reduction of the structural XAS oscillations obtained on increasing temperature is clearly visible, already starting at the edge.

3. XAS data analysis

Experimental XAS data have been analysed with an advanced technique, using theoretical calculations of the x-ray absorption cross-section in the framework of the GNXAS method (for details see [19–21]). The method is based on the comparison in the energy space of the experimental signal, $\alpha_{exp}(E)$, and the theoretical one, $\alpha_{mod}(E)$. A χ^2-like function [19, 20] is minimized, optimizing the parameters defining the model absorption spectrum $\alpha_{mod}(E)$. Inclusion of L_2- and L_1-edge spectra in the framework of the multiple-edge-fitting procedure turned out to be not particularly important for improving the quality of the structural results. Therefore, only the L_3-edge data were analysed in this work.

The atomic background associated with the L_3-edge absorption spectra contains important features associated with the opening of double-electron channels [22]. These features are clearly observed in liquid Pb at high temperature as well as in PbO at the same energies and are intrinsic features in the L_3-edge XAFS spectra. Therefore, the model absorption signal was built accounting for those multi-electron-excitation channels contributing to the L_3-edge atomic background. In particular, we found that there are important contributions due to the [2p5d] and [2p5p] channels around 40 and 110 eV above the edge besides the main [2p4f] discontinuity [22] observed at about 180 eV excess energy. These background features are located in the useful energy range for XAFS structural refinement; therefore their proper inclusion is absolutely necessary for a reliable structural refinement using an extended energy range for solid Pb and any other Pb compound.

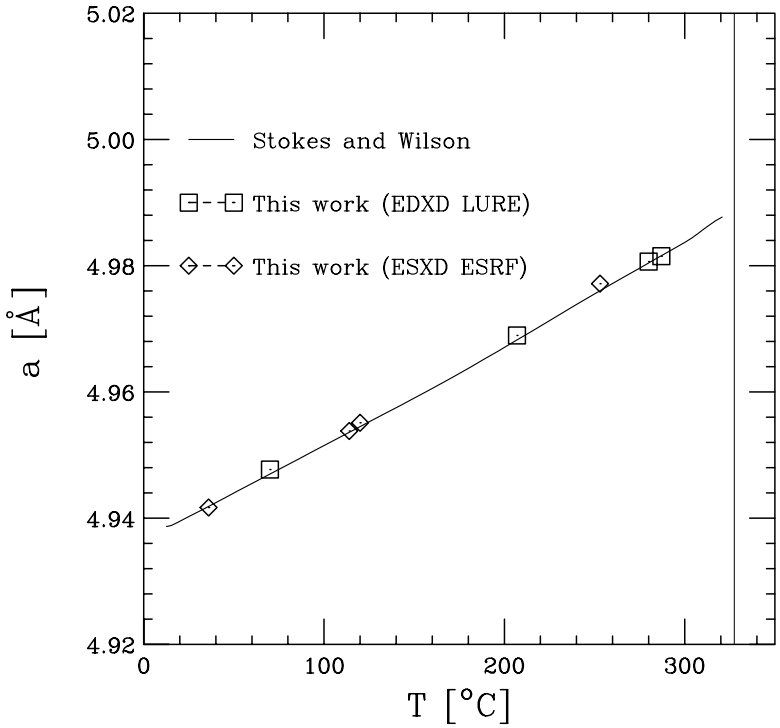

Figure 2. The lattice parameter obtained by EDXD (LURE) and ESXD (ESRF) for Pb–C and Pb–BN powder mixtures compared with the currently accepted thermal expansion curve (see [25]).

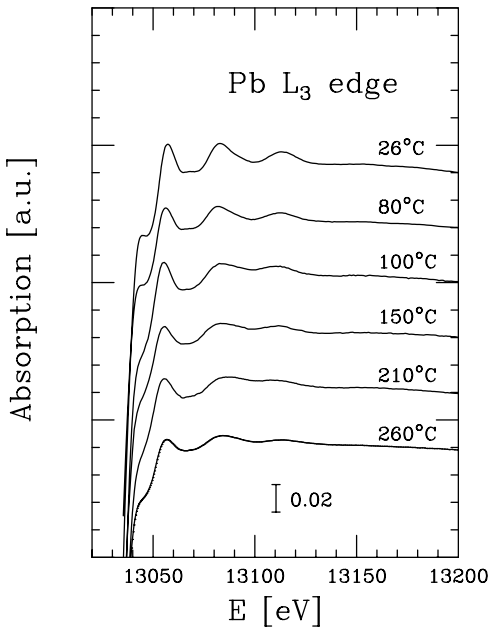

Figure 3. L_3 near-edge XAFS spectra of solid Pb at various temperatures.

The L_3-edge multiple-scattering $\gamma^{(n)}$-signals were calculated using the muffin-tin approximation and the Hedin–Lundqvist self-energy (see [19, 20] and references therein for details). The muffin-tin radii were about 1.39 Å corresponding to about 80 electrons for the integral of the charge density. Both the s and d final channels were taken into account in the calculation of the two- and three-body $\gamma^{(n)}$-signals associated with the corresponding atomic configurations in the fcc lattice.

In the range of temperatures under consideration, the dominant structural contributions in the solid Pb XAS spectra are those due to the first-neighbour distribution. Therefore, only the first-shell two-body signal $\gamma^{(2)}$ was used in the XAS data analysis.

The first-shell distribution was modelled using a Γ-like function which has already been shown to be able to reproduce the shape of the first radial distribution peak for several important systems (see [3, 4, 9, 26] and references therein).

The bond-length probability density $p(r)$ is then given by [26]

$$p(r) = \frac{2N}{\sigma|\beta|\Gamma(4/\beta^2)}\left(\frac{4}{\beta^2} + \frac{2(r-R)}{\sigma\beta}\right)^{4/\beta^2-1} \exp\left[-\left(\frac{4}{\beta^2} + \frac{2(r-R)}{\sigma\beta}\right)\right]. \tag{1}$$

Equation (1) is defined for $(r - R)\beta > -2\sigma$ and depends on only four parameters: N, the number of neighbours (coordination number); R, the average distance; σ^2, the distance variance (the so-called Debye–Waller-like disorder factor); β, the dimensionless asymmetry parameter. Γ is the Euler function. In the present case $N = 12$, as imposed by the crystal structure. An important advantage of equation (1) is that the β-parameter, directly related to the third cumulant K_3 ($\beta = K_3/\sigma^3$), defines the asymmetric shape and all the higher-order cumulants of the $p(r)$ continuously through the Gaussian limit $\beta = 0$.

The model signal $\alpha_{mod}(E)$ depends also on non-structural parameters such as S_0^2 (amplitude reduction factor) and E_o (onset energy of the empty levels) [19, 20]. The S_0^2-parameter was refined at room temperature and kept constant within narrow limits (0.88 ± 0.02) at all temperatures. The E_o-parameter was found in all cases to be about 1 eV above the edge energy, defined as the maximum of the spectrum derivative near the threshold.

The results of the XAS data analysis are shown in figure 4, where several $k\chi(k)$-spectra and best-fit calculated spectra are compared as a function of the temperature (k is the photoelectron wavevector).

The resulting best-fit parameters defining the first-shell distribution are reported in table 1. The typical uncertainty for the average distances is below 0.01 Å. The absolute error on bond variances is of the order of 10%. It has to be noted, however, that this uncertainty has been obtained taking into account its correlation with the amplitude factors S_0^2. The relative uncertainty on the temperature behaviour is reduced of a factor of ten. Therefore the trend of σ^2 as a function of temperature is measured with very good accuracy. The skewness β is also measured with reasonable accuracy (around 20%). The overall consistency of the present XAS structural results can be appreciated looking at the monotonic increase with temperature of the parameters reported in table 1.

4. Molecular dynamics simulations

4.1. Interaction models

Realistic structural models for solid lead can be obtained using MD and suitable parametrizations for the interaction potentials. In this work we will consider the following interaction models:

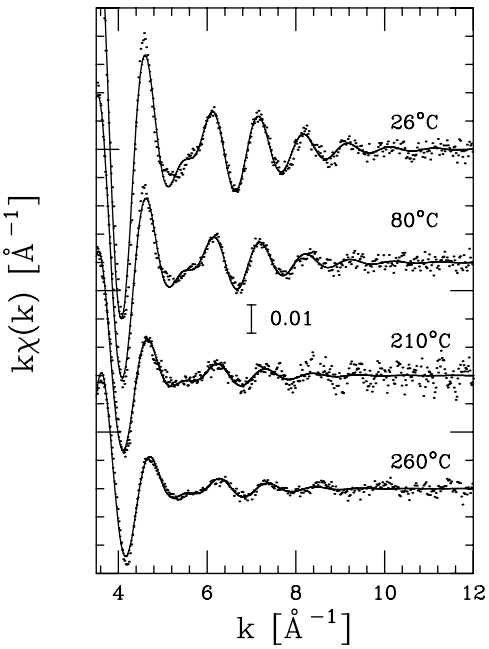

Figure 4. Comparison between experimental (dots) and calculated XAFS spectra for solid Pb at various temperatures.

Table 1. Structural parameters R, σ^2, β, and $K_3 = \beta\sigma^3$ defining the first-shell distribution, obtained from XAS spectra using the GNXAS method. Statistical error bars are shown in brackets.

T (°C)	R (Å)	σ^2 (Å^2)	β	K_3 (Å^3)
26(1)	3.496(8)	0.029(3)	0.32(6)	1.6×10^{-3}
79(2)	3.504(8)	0.035(3)	0.34(6)	2.2×10^{-3}
102(2)	3.506(9)	0.038(3)	0.35(7)	2.6×10^{-3}
150(2)	3.514(9)	0.044(4)	0.37(7)	3.4×10^{-3}
210(2)	3.524(10)	0.051(5)	0.44(8)	5.1×10^{-3}
260(2)	3.532(10)	0.055(6)	0.45(9)	5.8×10^{-3}

(I) An EA potential [12–15], parametrized by ourselves [27]. EA potentials are formulated within the density functional theory, and can be constructed for both effective-medium and quasi-atom versions. The parametrization of the realistic EA potentials is based on known physical values for the equilibrium atomic volume, bulk modulus, and cohesive energy, and suitable treatment of the electron density and repulsive pair potentials. Our new parametrization method, based on an inversion technique, will be briefly described in section 4.2.

(II) A TB [28] potential of the form

$$V(r_i) = -\left[\sum_j \xi^2 \exp\left(-2q\left(\frac{r_{ij}}{r_0} - 1\right)\right)\right]^{1/2} + \sum_j A \exp\left(-p\left(\frac{r_{ij}}{r_0} - 1\right)\right), \tag{2}$$

where $r_{ij} = |\vec{r}_i - \vec{r}_j|$ is the distance between the ith and jth sites at $\vec{r}_i$ and $\vec{r}_j$, respectively, and r_0 is the first-neighbour distance in the lattice. In the first attractive many-body term in equation (2), ξ is an effective hopping integral, and q describes its dependence on the

relative interatomic distance. According to [28] the values of ξ and q for Pb are equal to 0.914 and 3.648 eV, respectively. The second, repulsive component of (2) is written simply as a pairwise sum of the Born–Mayer ion–ion repulsive exponentially decaying terms. For lead, we have $A = 0.098$ and $p = 9.576$ eV.

(III) An empirical two-body potential proposed originally for liquid lead by Dzugutov, Larsson and Ebbsjo (DLE) [29], and determined by a careful fitting of the MD results to the static structural factor $S(k)$ at 623 K (23 K above the melting temperature). The DLE potential contains hard-core and soft-core repulsion terms, and an oscillatory long-range Friedel component, and has the following form:

$$\begin{aligned} V(r) &= V_1(r) + V_2(r) + V_3(r), \\ V_1(r) &= \begin{cases} a_1(b_1/r^{12})\exp[(r-c_1)^{-1}], & r < c_1, \\ 0, & r \geqslant c_1, \end{cases} \\ V_2(r) &= \begin{cases} a_2(b_2/r - c_2)\exp[(r-b_2)^{-1}], & r < b_2, \\ 0, & r \geqslant b_2, \end{cases} \\ V_3(r) &= a_3 r^{-3}\cos(2K_F r) \end{aligned} \tag{3}$$

with the following values for the parameters: $a_1 = 102.5$ meV, $b_1 = 3.284$ Å, $c_1 = 5.72$ Å, $a_2 = 90$ meV, $b_2 = 4.83$ Å, $c_2 = 0.5$ Å, $a_3 = 418.3$ meV Å^3, $K_F = 1.5417$ Å^{-1}. This potential is considered the more realistic one for liquid lead as shown in [30], but as it is a two-body potential it is not expected to reproduce the short-range structure in solid Pb.

4.2. Construction of the embedded-atom potential

We present the main guidelines for our new approach [27] to the construction of the EA model potentials. In our method the EA functions are determined so as to reproduce simultaneously and exactly two energy–volume equations for two different metal structures. The method is thus an extension of the inversion technique proposed by Carlsson and co-workers [31], where the resulting pair potential reconstructs only one given energy–volume equation (hereafter called the 'state equation'). Previously, the inversion technique has been applied not only to the construction of pair potentials [18, 32–34], but also to EA potentials [35–37], although always from a single state equation.

In the EA approach [13, 14], the total energy of the metallic system is a sum of the energy necessary to embed each atom in the background electron density created by neighbouring atoms (the embedding energy) and the energy due to two-body interactions. The atomic charge density is taken from first-principles calculations. The host density ρ_i is approximated by superimposing the contributions of all the atoms surrounding atom i, $\rho_i = \sum_{j\neq i}\phi(r_{ij})$, where $\phi(r_{ij})$ is the electron density of atom j projected on atom i. The input data for our parametrization procedure are two state equations $E_\alpha(V)$ given for two structures $\alpha = 1, 2$ of different symmetries and the atomic charge density $\phi(r)$. Using these data we construct the embedding function and the pair potential function in the way described below.

The cohesive energy per unit cell as a function of atomic volume for lattice α is given by

$$E_\alpha(V) = \tfrac{1}{2}\sum_{i}^{N_\alpha}\sum_{j\neq i}\Phi(r_{ij}^\alpha) + \sum_{i}^{N_\alpha}\chi\left[\sum_{j\neq i}\phi(r_{ij}^\alpha)\right], \tag{4}$$

where V is the atomic volume, i refers to the atoms in the unit cell, j is referred to the atoms in the whole crystal, respectively, r_{ij}^α are the distances between atoms i and j in lattice α, $\Phi(r_{ij}^\alpha)$

is the pair potential, $\chi(\rho_i)$ is the embedding function, N_α is the number of atoms in the unit cell of lattice α.

The interatomic distance r_{ij} for both lattices may be expressed as a function of atomic volume and subsequent shell distances:

$$r_{ij}^{\alpha} = r_0^{\alpha}\left(\frac{V}{V_0}\right)^{1/3} a_s^{\alpha} \tag{5}$$

where s is an index of a neighbouring shell, r_0^{α} is the first-neighbour distance, V_0 is the equilibrium volume, and a_s^{α} is the ratio of the sth-neighbour distance to the first-neighbour distance.

Taking into account (5), equation (4) can be rewritten as

$$E_\alpha(V) = \frac{1}{2}\sum_s W_s^{\alpha}\Phi\left(r_0^{\alpha}\left(\frac{V}{V_0}\right)^{1/3} a_s^{\alpha}\right) + \chi^{\alpha}\left[\frac{1}{N_\alpha}\sum_s W_s^{\alpha}\phi\left(r_0^{\alpha}\left(\frac{V}{V_0}\right)^{1/3} a_s^{\alpha}\right)\right] \tag{6}$$

where W_s is the number of neighbours in a shell s. The functions χ^{α} are defined by

$$\chi^{\alpha}\left[\frac{1}{N_\alpha}\sum_s W_s^{\alpha}\phi\left(r_0^{\alpha}\left(\frac{V}{V_0}\right)^{1/3} a_s^{\alpha}\right)\right] = \sum_i^{N_\alpha}\chi\left[\sum_{j\neq i}\phi(r_{ij}^{\alpha})\right].$$

The difference $E_{diff}(V) = E_1(V)/N_1 - E_2(V)/N_2$ between the energies per atom calculated for the two lattices, expressed in terms of the atomic volume, is

$$\begin{aligned} E_{diff}(V) = {} & \frac{1}{2N_1}\sum_s W_s^1\Phi\left(r_0^1\left(\frac{V}{V_0}\right)^{1/3} a_s^1\right) - \frac{1}{2N_2}\sum_s W_s^2\Phi\left(r_0^2\left(\frac{V}{V_0}\right)^{1/3} a_s^2\right) \\ & + \frac{1}{N_1}\chi^1\left[\frac{1}{N_1}\sum_s W_s^1\phi\left(r_0^1\left(\frac{V}{V_0}\right)^{1/3} a_s^1\right)\right] \\ & - \frac{1}{N_2}\chi^2\left[\frac{1}{N_2}\sum_s W_s^2\phi\left(r_0^2\left(\frac{V}{V_0}\right)^{1/3} a_s^2\right)\right]. \end{aligned} \tag{7}$$

Since the arguments of the functions χ^1 and χ^2 in (7) do not differ remarkably, we have

$$\frac{1}{N_1}\sum_s W_s^1\phi\left(r_0^1\left(\frac{V}{V_0}\right)^{1/3} a_s^1\right) \approx \frac{1}{N_2}\sum_s W_s^2\phi\left(r_0^2\left(\frac{V}{V_0}\right)^{1/3} a_s^2\right),$$

and thus

$$\frac{1}{N_1}\chi^1(\rho) \approx \frac{1}{N_2}\chi^2(\rho),$$

which simplifies (7) to

$$E_{diff}(V) \approx \sum_s^{M_1}\frac{1}{2N_1}W_s^1\Phi\left(r_0^1\left(\frac{V}{V_0}\right)^{1/3} a_s^1\right) - \sum_s^{M_2}\frac{1}{2N_2}W_s^2\Phi\left(r_0^2\left(\frac{V}{V_0}\right)^{1/3} a_s^2\right), \tag{8}$$

where M_1 and M_2 are the numbers of coordination shells included in a sphere of radius r_{cut} for lattices 1 and 2, respectively. Using

$$K_s = \frac{1}{N_1}W_s^1, \qquad K_{s+M_1} = -\frac{1}{N_2}W_s^2, \qquad b_s = a_s^1, \qquad b_{s+M_1} = \frac{a_s^2}{r_0^1}r_0^2, \tag{9}$$

equation (8) becomes

$$E_{diff}(V) \approx \frac{1}{2}\sum_{s}^{M_1+M_2} K_s \Phi\left(r_0^1\left(\frac{V}{V_0}\right)^{1/3} b_s\right). \tag{10}$$

Now the pair potential Φ can be constructed using the lattice inversion technique [31]. Once Φ has been calculated, the embedding function χ can be determined. Subtracting the energy related to the pair potential from the cohesive energy $E_1(V)$, we get the embedding energy:

$$E_{emb}(V) = \chi(\rho(V)) = E_1(V) - \frac{1}{2}\sum_{s} W_s^1 \Phi\left(r_0\left(\frac{V}{V_0}\right)^{1/3} a_s^1\right), \tag{11}$$

where the charge-density function $\rho(V)$ is a superposition of the atomic charge-density functions ϕ:

$$\rho(V) = \sum_{s} \frac{1}{N_1} W_s^1 \phi\left(r_0\left(\frac{V}{V_0}\right)^{1/3} a_s^1\right).$$

Elimination of volume V from equation (11) gives the embedding function $\chi(\rho)$.

The embedding function is calculated from the state equation $E_1(V)$, and the EA potential exactly reconstructs this equation. Due to the approximations used in our procedure, the state equation reconstructed for lattice 2 differs from the initial $E_2(V)$. The error mainly depends on the behaviour at large volumes of $E_{diff}(V)$. For $E_{diff}(V)$ quickly going to 0 the error is rather small. In our calculations performed for solid Pb, the error is about 10% of the initial $E_{diff}(V)$. For some applications the accuracy of this procedure could be insufficient, and a correction scheme is necessary. We have then used the following self-consistent correction procedure:

(1) Determine the pair potential Φ and embedding function χ from the state equations $E_1(V)$ and $E_2(V)$ as described above.
(2) Calculate the correction function $E_{cor}(V)$ defined as the difference of the original $E_2(V)$ and the state equation for lattice 2, reconstructed by the current potential.
(3) Add $E_{cor}(V)$ to $E_{diff}(V)$.
(4) Recalculate the EA functions using E_1 and the new E_{diff}.
(5) Determine a new correction function $E_{cor}(V)$ using the current potential, add it to the old one, and repeat the extraction (go to step 4).

This procedure can be executed until the calculated and initial state equations $E_2(V)$ are close enough. In every cycle $E_1(V)$ is always exactly reconstructed. The error in the reconstruction of $E_2(V)$ is eliminated by the proper adjustment of the correction E_{cor} of the state equation difference E_{diff}. In the present calculations for solid Pb, a few cycles are sufficient to reach 10^{-4} eV accuracy.

The pair potential and embedding functions for Pb have been determined from empirical state equations (constructed on the basis of experimental work [38–41]), and from the atomic charge density determined from first-principles calculations (using the programme of Liberman and co-workers [42]). Two different lattices, fcc and bcc, were considered in the construction of the EA potential following the above-mentioned procedure. The energy difference between the two lattices was approximated for low volumes by a linear function, which smoothly changes into an exponential function for greater volumes. The parameters of these functions have been constrained by using values of equilibrium atomic volume, cohesive energy, and the bulk modulus of $E_2(V)$, as well as the volume for which the energies of bcc and fcc phases are equal (extrapolated to 0 K). The functions $\chi(\rho)$, $\Phi(r)$, and $\phi(r)$ determined using this procedure have been also used to calculate some bulk and defect properties of solid lead, and good agreement with experimental values of the elastic constants C_{11}, C_{12}, and C_{44} has been obtained [27].

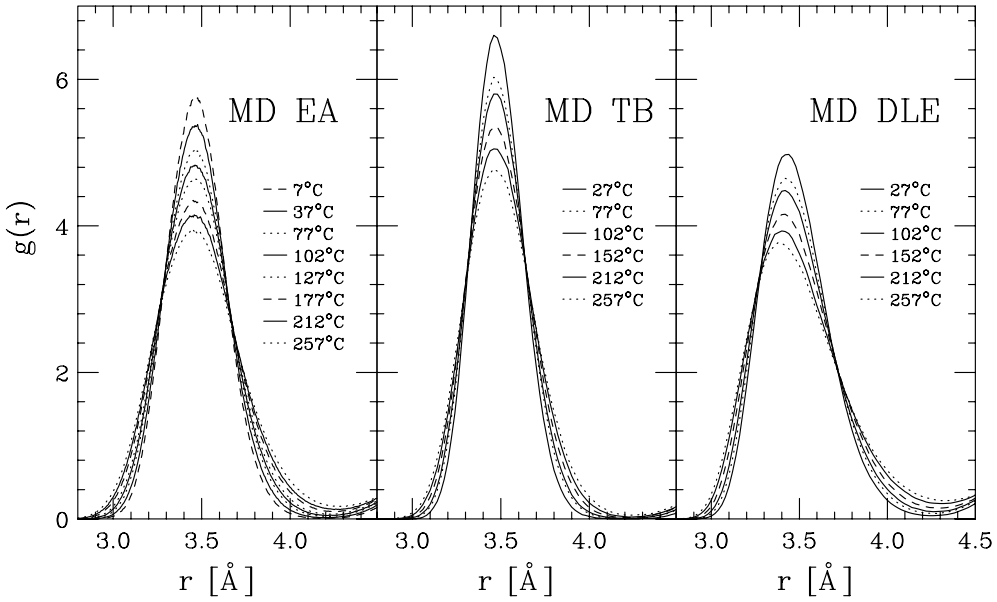

Figure 5. The first $g(r)$ peak as determined by MD simulations using the EA, TB, and DLE models (see the text) for solid Pb as a function of the temperature.

In the next section we describe some computational details and characteristics of the MD simulations performed using the three interaction models mentioned above.

4.3. Molecular dynamics simulations and overall characteristic of the results

Classical MD simulations for 864 Pb atoms with TB and DLE potentials were performed in the *NVE* ensemble. For these potentials, the use of constant-volume conditions appeared necessary to avoid unacceptable deviations of the density from the known experimental values, even if the internal pressures calculated using the virial theorem in NpT calculations turned out to be reasonably small. On the other hand, our new EA interaction model allowed us to perform successful zero-external-pressure simulations, still retaining the correct density. The NpT simulations with the EA potential were performed using 1372 atoms. The calculations were performed using the DL_POLY program [43] at several temperatures between 7 and 257 °C. In this temperature range quantum effects related to the zero-point vibration are practically negligible as all of the vibrational modes can be thermally excited (the Debye temperature of Pb is about 105 K).

Pair distribution functions $g(r)$ were calculated over 5000 or 10 000 time steps of sampling runs (time step $t = 5 \times 10^{-15}$ s). The first peak of the $g(r)$ is reported as a function of temperature in figure 5. The three panels of figure 5 contain the results related to the EA, TB, and DLE models. The general trend is obviously a broadening of the peak at increasing temperatures but important differences can be observed for the different potentials. Vibrational amplitudes in the DLE models are higher than in the other two models and the first-neighbour peak is broader and asymmetrically merging with the second shell at higher distances. The $g(r)$s associated with the EA and TB models are qualitatively similar, but the latter is narrower as a consequence of the different shape for the interaction.

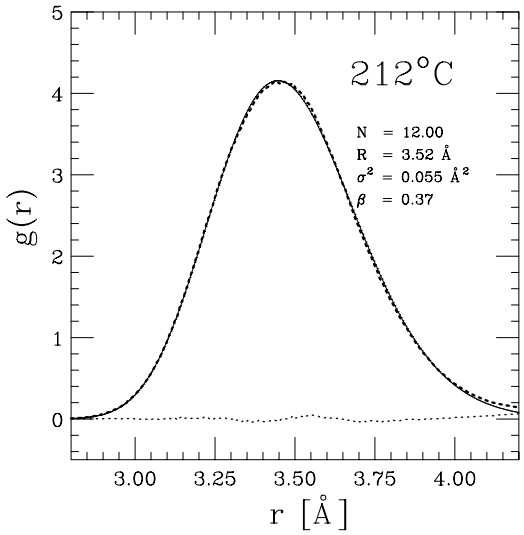

Figure 6. The first-neighbour $g(r)$ peak obtained by EA simulation at 212 °C (solid curve) compared with a Γ-like function (bold dots) calculated using best-fit parameters shown in the figure. The agreement is excellent, as shown by the residual curve (dots).

A more quantitative understanding of the characteristics of the structural models can be obtained by using a suitable parametrization for the first-shell peak shape. A suitable function able to reproduce quite accurately the first-shell distribution in systems at moderately high temperatures is the Γ-like function discussed in section 3. The bond-length probability density, expressed by equation (1), was then used to model the shape of the first peak of the pair distribution functions shown in figure 5.

We have found that the shape of the first peak can be accurately modelled using the Γ-like function, as shown in previous cases (see for example [1,3,9]). A typical first-neighbour peak modelled using best-fit parameters of a Γ-like function is shown in figure 6, where the accuracy of the present parametrization can be appreciated. Best-fit average distance R, variance σ^2, skewness β, and third cumulant $K_3 = \beta\sigma^3$ for the EA, TB, and DLE model potentials are reported in table 2. The large values of the first-neighbour distance variance, related to the width of the peak of the pair distribution and to the vibrational amplitudes, indicate, *a posteriori*, that classical MD simulations can be safely used in this temperature range.

5. Results and discussion

Structural results obtained using MD simulations reported in the preceding section will be now compared with XAS experimental data presented in section 3.

In figure 7 the average first-neighbour distance R obtained from the XAFS is compared with the results of the MD simulations, and with the thermal expansion measured by means of diffraction. The average interatomic distance is slightly longer than the site-to-site distance obtained by rescaling the cell parameter a measured by means of diffraction. This is a well-known result due to the positive contribution of the vibrations perpendicular to the bond direction (see for example [26] and references therein). Due to the increase in the vibrational amplitudes with temperature, the average interatomic distance expands more rapidly than the cell side (thermal expansion). It is clear that the DLE pair potential, parametrized for liquid

Table 2. Structural parameters R, σ^2, β, and $K_3 = \beta\sigma^3$ defining the first-shell distribution, obtained from MD simulations using the EA, TB, and DLE potentials.

	T (°C)	R (Å)	σ^2 (Å^2)	β	K_3 (Å^3)
EA	7	3.491	0.027	0.23	1.0×10^{-3}
	37	3.495	0.031	0.25	1.4×10^{-3}
	77	3.499	0.036	0.27	1.8×10^{-3}
	102	3.503	0.039	0.29	2.2×10^{-3}
	127	3.507	0.043	0.30	2.7×10^{-3}
	177	3.514	0.050	0.34	3.8×10^{-3}
	212	3.520	0.055	0.37	4.8×10^{-3}
	257	3.528	0.062	0.40	6.2×10^{-3}
TB	27	3.499	0.021	0.25	0.8×10^{-3}
	77	3.505	0.025	0.27	1.1×10^{-3}
	102	3.507	0.027	0.28	1.2×10^{-3}
	152	3.514	0.032	0.32	1.8×10^{-3}
	212	3.521	0.037	0.33	2.4×10^{-3}
	257	3.527	0.042	0.36	3.1×10^{-3}
DLE	27	3.507	0.040	0.56	4.5×10^{-3}
	77	3.514	0.047	0.60	6.1×10^{-3}
	102	3.518	0.052	0.62	7.3×10^{-3}
	152	3.527	0.062	0.68	11×10^{-3}
	212	3.537	0.072	0.73	14×10^{-3}
	257	3.544	0.081	0.77	18×10^{-3}

Pb, reproduces rather poorly the experimental curve, while both TB and EA models give an average distance in good agreement with present experimental data. The dashed curve reported in figure 7 refers to previous XAFS experimental results obtained using an alternative data-analysis technique based on the cumulant expansion [11]. The first four cumulants are given in that paper and it is possible to make a direct comparison with known thermal expansion curves, realistic MD simulations, and present XAFS results. As noted also by the authors themselves, the thermal expansion turned out to be underestimated. In fact, the average linear thermal expansion coefficient α in the present temperature range is $\alpha \sim 3.2 \times 10^{-5}$ K^{-1} while previous XAFS data gave $\alpha \sim 2.3 \times 10^{-5}$ K^{-1}. The dashed line shown in figure 7 is calculated using the slope indicated in the previous work and the current room temperature distance value obtained by diffraction, because only variations of distances are measured in the original paper.

In figure 8 we report the first-neighbour distance variance (upper panel) and skewness (lower panel). The DLE potential, as expected, is too soft and cannot reproduce the actual values of the distance variance and skewness. The distance variance given by the TB model ($\times$) is underestimated while the EA model ($\boxdot$) gives variance values in much better agreement with present experimental data. Moreover, variance and skewness derived by the previous XAFS work [11] are in good agreement with present determination, showing that quite accurate estimates for the second and third cumulants were given using standard procedures.

The pair distribution function can be easily reconstructed using equation (1) and the best-fit structural parameters obtained for solid Pb. In figure 9 we show the first-neighbour $g(r)$ as a function of temperature as determined from the XAFS. The distribution broadens with increasing temperature, with a shortening of the peak maximum distance

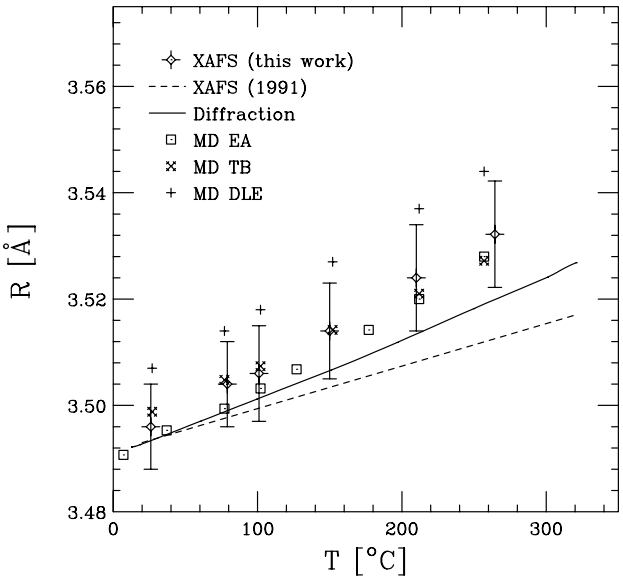

Figure 7. Average first-neighbour interatomic distances measured by XAFS and simulated by MD are reported as a function of temperature. Diffraction data (continuous line) measuring the average site-to-site distance $a/\sqrt{(2)}$ are reported for comparison. Previous XAFS data reported in [11] are also shown.

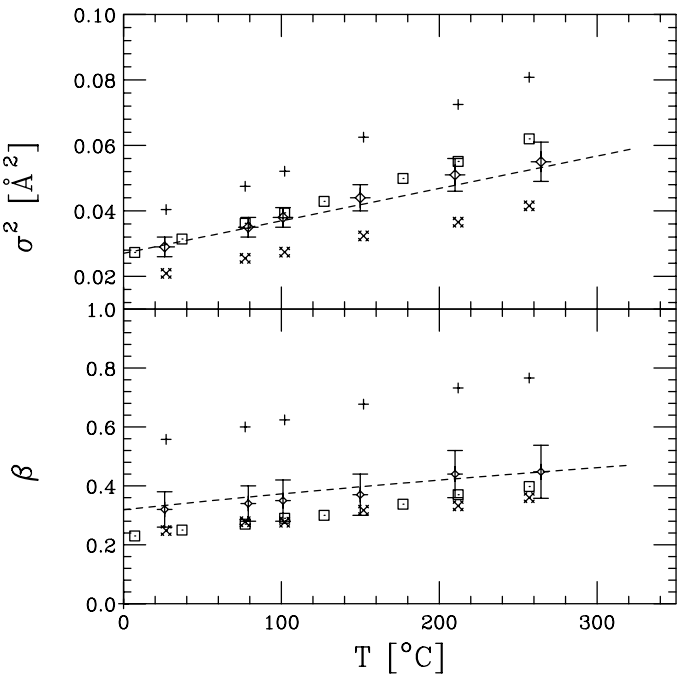

Figure 8. First-neighbour variance σ^2 and skewness β measured from the XAFS and simulated by MD are reported as a function of temperature (same key as for figure 7).

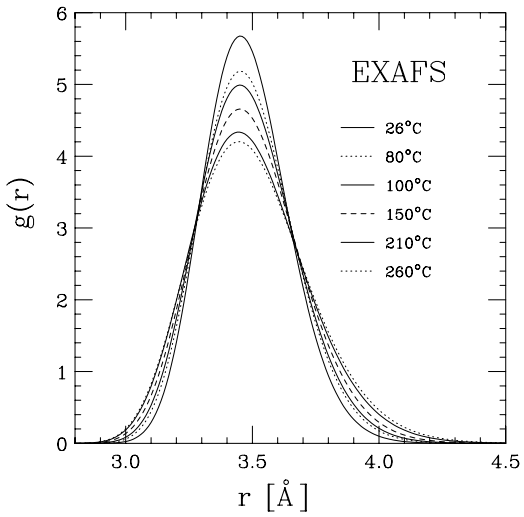

Figure 9. First-neighbour $g(r)$ peaks as determined by XAFS analysis at various temperatures.

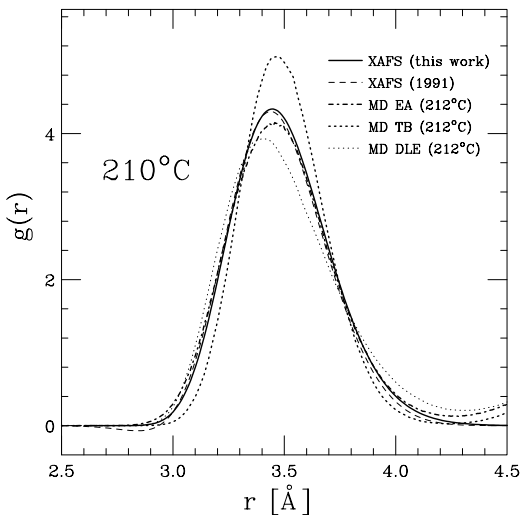

Figure 10. Comparison of short-range $g(r)$s at 210 °C obtained from XAS analysis (dashed curve: [11]; solid curve: this work) and MD simulations using the EA (dot–dashed curve), TB and DLE (dotted curves) interatomic potentials.

accompanied with the increase of the average distance following the thermal expansion. The pair distribution at 210 °C measured from the XAFS is compared with the corresponding ones obtained by using TB, EA, and DLE models in figure 10. The EA model is in very good agreement with experimental XAFS data while the TB one underestimates the vibrational broadening at the same temperature. On the other hand, the pairwise DLE potential clearly overestimates the width and asymmetry of the first-neighbour distribution.

The dashed curve (XAFS) shown in figure 10 is a possible reconstruction of the $g(r)$ function made on the basis of the previous XAFS study [11] using a simple anharmonic one-

dimensional potential. In the light of what we have shown about interaction potentials in solid metals, the 'potential' presented in [11] cannot be regarded as a true interatomic potential, but is just an effective function useful for that kind of XAFS data analysis. In matter of fact, the pair distribution function that was reconstructed on the basis of equation (19) in [11] is not positive definite and can give completely meaningless results when higher-order cumulants are included. This is just a consequence of the difficulty in using the cumulant expansion, which can be very slowly convergent. However, a reasonable result can be obtained by including only the first three cumulants and the appropriate density. In fact, the dashed curve in figure 10 has been calculated using only the first three cumulants published in [11]. It must be remarked that this seems to be the only way to derive reasonable results for the $g(r)$ from the previous XAFS data, because addition of the fourth cumulant published in [11] leads to a completely meaningless shape for $g(r)$. The calculated $g(r)$ shown in figure 10, which must be a positive-definite function, is still negative in the region near the rise of the first peak, but turns out to be quite accurate elsewhere, as compared with both current experimental XAFS data and realistic TB and EA models.

6. Conclusions

Accurate Pb L_3 XAFS measurements of Pb grains dispersed into BN or graphite matrices were performed at the BM29 beamline (ESRF) in the 26–260 °C range of temperatures. EDXD and ESXD measurements were also performed, measuring the thermal expansion properties of the samples and keeping their purity under control. XAFS data were analysed using the GNXAS data-analysis method [19–21], taking into account double-electron-excitation channels and modelling the first-shell distribution as a Γ-like function. In fact, the harmonic approximation does not hold in solid Pb even at moderate temperature and the Gaussian model is not accurate enough.

The first-shell distribution was calculated by MD simulation using different approximations for the interatomic potentials (DLE, TB, EA) [27–29]. The DLE approximation is a two-body potential originally designed for explaining the structure of liquid Pb. The TB and EA ones are many-body potentials designed to reproduce specific long-range solid-state properties of solid Pb. The first-shell peaks of the MD simulations were accurately approximated by Γ-like functions with suitable parameters. Direct comparison with XAFS experimental results showed that the DLE potential is too soft for describing solid Pb. The distance variance σ^2 and skewness β of the first neighbours turned out to be overestimated. The average interatomic distance is also overestimated within the DLE model, due to the positive contribution of the vibrations perpendicular to the bond direction. The TB and EA potentials, however, are both compatible with XAFS data as regards the average distance and skewness of the first neighbours. The distance variance given by the TB model turns out to be underestimated. The EA model provides variance values that are in agreement with the experimental ones. This last interaction model is therefore found to be able to reproduce completely the short-range structure as probed by XAFS.

Previous XAFS results [11] on solid Pb have been re-examined in the light of the present data; this has shown that existing disagreements of XAFS data with known thermal expansions are now removed, while the variance and skewness of the first-neighbour distribution are substantially confirmed. The pair distribution function derived using the one-dimensional effective potential described in previous work is shown to be not positive definite (using more than two cumulants) and its shape is too sensitive to the values of the cumulants. In particular, we emphasize that the message that can be inferred from previous XAFS work, i.e. that a simple one-dimensional potential and cumulant expansion treatment leads

to accurate and physically meaningful results, can be misleading. The potentials to be used for metals like Pb are three-dimensional and contain essential many-body contributions, while cumulant expansions must be used with caution because they can lead to inaccurate or physically meaningless results (negative and nonphysical shapes for the $g(r)$). These facts should be taken into account in any serious attempt to study the local structure of metals using XAFS.

The methods of XAFS data analysis and the results obtained in this paper are presented with the aim of reconciling this technique with current strategies for understanding the properties of metals and showing the potential of XAFS for use in testing the interaction models and studying the local structure of systems under high-temperature conditions.

Acknowledgments

We would like to thank the ESRF BM29 (Grenoble) and the LURE DW11 (Orsay) staff, in particular A Filipponi, S De Panfilis and J P Itié, for their expertise and collaboration in setting up the experiments. The TASK Computer Centre in Gdansk is gratefully acknowledged for allowing the use of their multiprocessor systems. The work was partially sponsored by INFM and the Polish Committee for Scientific Research, grant No 7 T08D 009 20.

References

[1] Di Cicco A, Filipponi A, Itié J P and Polian A 1996 *Phys. Rev.* B **54** 9086
[2] Yokoyama T, Ohta T and Sato H 1997 *Phys. Rev.* B **55** 11 320
[3] Di Cicco A, Rosolen M J, Marassi R, Tossici R, Filipponi A and Rybicki J 1996 *J. Phys.: Condens. Matter* **8** 10 779
[4] Di Cicco A, Minicucci M and Filipponi A 1997 *Phys. Rev. Lett.* **78** 460
[5] Edwards A B, Tildesley D J and Binsted N 1997 *Mol. Phys.* **91** 357
[6] Aquilanti G, Di Cicco A, Minicucci M, Filipponi A and Rybicki J 1999 *J. Synchrotron Radiat.* **6** 251
[7] Minicucci M and Di Cicco A 1997 *Phys. Rev.* B **56** 11 456
[8] Di Cicco A and Minicucci M 1999 *J. Synchrotron Radiat.* **6** 255
[9] Di Cicco A, Aquilanti G, Minicucci M, Filipponi A and Rybicki J 1999 *J. Phys.: Condens. Matter* **11** L43
[10] Laskowski R, Rybicki J, Chybicki M and Di Cicco A 2000 *Phys. Status Solidi* **217** 737
[11] Stern E A, Livins P and Zhang Z 1991 *Phys. Rev.* B **43** 8850
[12] Daw M S and Baskes M I 1983 *Phys. Rev. Lett.* **50** 1285
[13] Daw M S and Baskes M I 1984 *Phys. Rev.* B **29** 6443
[14] Daw M S 1989 *Phys. Rev.* B **39** 7441
[15] Daw M S, Foiles S M and Baskes M I 1993 *Mater. Sci. Rep.* **9** 251
[16] Finnis M W and Sinclair J E 1984 *Phil. Mag.* A **50** 45
[17] Sutton A P and Chen J 1990 *Phil. Mag. Lett.* **61** 139
[18] Chen N 1990 *Phys. Rev. Lett.* **64** 1193
[19] Filipponi A, Di Cicco A and Natoli C R 1995 *Phys. Rev.* B **52** 15 122
[20] Filipponi A and Di Cicco A 1995 *Phys. Rev.* B **52** 15 135
[21] Filipponi A and Di Cicco A 2000 *TASK Q.* **4** 575
[22] Di Cicco A and Filipponi A 1994 *Phys. Rev.* B **49** 12 564
[23] Filipponi A and Di Cicco A 1994 *Nucl. Instrum. Methods Phys. Res.* B **93** 302
[24] Filipponi A, Borowski M, Bowron D T, Ansell S, De Panfilis S, Di Cicco A and Itié J P 2000 *Rev. Sci. Instrum.* **71** 2422
[25] Stokes A R and Wilson J C 1941 *Proc. Phys. Soc.* **53** 517
[26] Filipponi A and Di Cicco A 1995 *Phys. Rev.* B **51** 12 322
[27] Laskowski R 2000 *Phys. Status Solidi* b **222** 457
[28] Cleri F and Rosato V 1993 *Phys. Rev.* B **48** 22
[29] Dzugutov M, Larsson K and Ebbsjo I 1988 *Phys. Rev.* A **38** 3609
[30] Rycerz Z A and Jacobs P 1991 *Mol. Phys.* **74** 425

[31] Carlsson A E, Gelatt C D and Ehrenreich E 1980 *Phil. Mag.* A **41** 241
[32] Esposito B E, Carlsson A E, Ling D D, Ehrenreich H and Gelatt C D 1980 *Phil. Mag.* A **41** 251
[33] Mookerjee A, Chen N, Kumar V and Satter M A 1992 *J. Phys.: Condens. Matter* **4** 2439
[34] Chen N and Ren G 1992 *Phys. Rev.* B **45** 8177
[35] Xie Q and Chen N 1995 *Phys. Rev.* B **51** 15 856
[36] Xie Q and Huang M 1994 *J. Phys.: Condens. Matter* **6** 11 015
[37] Xie Q and Huang M 1994 *Phys. Status Solidi* b **186** 393
[38] Gschneidner K A Jr 1964 *Solid State Physics* vol 16 (New York: Academic) p 275
[39] Liu A Y, Garcia A, Cohen M L, Godwal B K and Jeanloz R 1991 *Phys. Rev.* B **43** 1795
[40] Mao H K, Wu Y, Shu J F, Hu J Z, Hemley R J and Cox D E 1990 *Solid State Commun.* **74** 1027
[41] Vohra Y K and Ruoff A L 1990 *Phys. Rev.* B **42** 8651
[42] Liberman D A, Cromer D T and Waber J T 1971 *Comput. Phys. Commun.* **2** 107
[43] http://www.dl.ac.uk/TCS/Software/DL_POLY/